**AGU** ADVANCING EARTH AND SPACE SCIENCE

# Geophysical Research Letters®

## Enhanced India-Africa Carbon Uptake and Asia-Pacific Carbon Release Associated With the 2019 Extreme Positive Indian Ocean Dipole

Jun Wang[1,2] ⓘ, Fei Jiang[1,2] ⓘ, Weimin Ju[1,2], Meirong Wang[3], Stephen Sitch[4] ⓘ, Vivek K. Arora[5], Jing M. Chen[6] ⓘ, Daniel S. Goll[7] ⓘ, Wei He[1,2] ⓘ, Atul K. Jain[8] ⓘ, Xing Li[9], Joanna Joiner[10] ⓘ, Benjamin Poulter[11], Roland Séférian[12] ⓘ, Hengmao Wang[1,2] ⓘ, Mousong Wu[1,2] ⓘ, Jingfeng Xiao[13] ⓘ, Wenping Yuan[14], Xu Yue[15] ⓘ, and Sönke Zaehle[16] ⓘ

[1]Jiangsu Provincial Key Laboratory of Geographic Information Science and Technology, International Institute for Earth System Science, Nanjing University, Nanjing, China, [2]Frontiers Science Center for Critical Earth Material Cycling, Nanjing University, Nanjing, China, [3]Joint Center for Data Assimilation Research and Applications/Key Laboratory of Meteorological Disaster, Ministry of Education/Joint International Research Laboratory of Climate and Environment Change (ILCEC)/ Collaborative Innovation Center ON Forecast and Evaluation of Meteorological Disasters, Nanjing University of Information Science and Technology, Nanjing, China, [4]College of Life and Environmental Sciences, University of Exeter, Exeter, UK, [5]Canadian Centre for Climate Modelling and Analysis, Environment and Climate Change Canada, Victoria, BC, Canada, [6]Department of Geography, University of Toronto, Toronto, ON, Canada, [7]Laboratoire des Sciences du Climat et de l'Environnement, CEA-CNRS-UVSQ-Université Paris-Saclay, Gif-sur-Yvette, France, [8]Department of Atmospheric Sciences, University of Illinois, Urbana, IL, USA, [9]Research Institute of Agriculture and Life Sciences, Seoul National University, Seoul, South Korea, [10]Laboratory for Atmospheric Chemistry and Dynamics, National Aeronautics and Space Administration (NASA) Goddard Space Flight Center (GSFC), Greenbelt, MD, USA, [11]Biospheric Sciences Laboratory, NASA Goddard Space Flight Center, Greenbelt, MD, USA, [12]CNRM, Université de Toulouse, Météo-France, CNRS, Toulouse, France, [13]Earth Systems Research Center, Institute for the Study of Earth, Oceans, and Space, University of New Hampshire, Durham, NH, USA, [14]School of Atmospheric Sciences, Southern Marine Science and Engineering Guangdong Laboratory (Zhuhai), Sun Yat-sen University, Zhuhai, China, [15]Jiangsu Key Laboratory of Atmospheric Environment Monitoring and Pollution Control, Collaborative Innovation Center of Atmospheric Environment and Equipment Technology, School of Environmental Science and Engineering, Nanjing University of Information Science and Technology (NUIST), Nanjing, China, [16]Max Planck Institute for Biogeochemistry, Jena, Germany

**Abstract** The 2019 extreme positive Indian Ocean dipole drove climate extremes over Indian Ocean rim countries with unclear carbon-cycle responses. We investigated its impact on net biome productivity (NBP) and its constituent fluxes, using the Global Carbon Assimilation System (GCASv2) product, process-based model simulations from TRENDYv9, and satellite-based gross primary productivity (GPP). By distinguishing two separate regions, the India-Africa and Asia-Pacific, GCASv2 indicated enhanced terrestrial carbon uptake of $0.23 \pm 0.20$ PgC and release of $0.38 \pm 0.15$ PgC, respectively, during September–December (SOND) 2019. These NBP anomalies had comparable magnitudes to those following the 2015 extreme El Niño which, however, caused the consistent carbon release in both regions. The TRENDYv9 model ensemble confirmed these NBP responses, albeit with smaller magnitudes. These regional NBP anomalies were related to soil moisture variations with a dominant role of GPP. Understanding the impact of IOD provides new insights into mechanisms driving interannual variations in regional carbon cycling.

**Plain Language Summary** The extreme Indian Ocean Dipole (IOD) can drive climate extremes, such as floods, heatwaves, droughts, and wildfires, over the Indian Ocean rim countries. However, responses of regional terrestrial carbon cycling to IOD remained unclear. We used the net biome productivity (NBP) from an atmospheric inversion and multiple terrestrial biosphere models to demonstrate an enhanced terrestrial carbon uptake and release over the India-Africa and Asia-Pacific regions, respectively, during the extreme positive IOD (September–December) in 2019. These IOD-induced regional NBP anomalies showed comparable magnitudes but different patterns to those following the 2015 extreme El Niño. Along with the more frequent extreme IOD under future greenhouse warming, IOD will be an important mechanism driving interannual variations in regional carbon cycling.

## 1. Introduction

The Indian Ocean Dipole (IOD) is an ocean-atmosphere coupled mode of variability that can directly influence climate variations on interannual timescales over the regions surrounding the Indian Ocean (Ashok et al., 2004; Behera et al., 2006; Cai et al., 2011; Saji & Yamagata, 2003; Saji et al., 1999). The climate impacts of IOD are known to be different from those induced by the El Niño-Southern Oscillation (ENSO) (Ashok et al., 2004; Cai et al., 2011; Saji & Yamagata, 2003). In a positive IOD (denoted as "pIOD"), the sea surface temperature (SST) initially cools off Sumatra-Java, enhancing the southeasterly trade winds. The anomalous southeasterly winds in turn reinforce the initial cooling through the enhanced upwelling and shoaling of the thermocline but accumulate the warm SST over the equatorial western Indian Ocean (Saji et al., 1999). These altered circulations in the ocean and atmosphere can cause climate extremes, such as floods, heatwaves, droughts, and wildfires (Ashok et al., 2003; Behera et al., 2005; Cai et al., 2009; Kim et al., 2019; Ummenhofer et al., 2009), over the Indian Ocean rim countries (IORC), exerting the concurrent and lagged abiotic stresses on regional ecosystems and terrestrial carbon fluxes.

More recently, an extreme pIOD event, one of the strongest in the last four decades, occurred in 2019 (Figure S1 in Supporting Information S1). It contributed to the megabushfires over the temperate forests in eastern Australia, releasing large amounts of carbon dioxide ($CO_2$) (Boer et al., 2020; Byrne et al., 2021; van der Velde et al., 2021; Wang et al., 2020). Concurrently, the Niño 3.4 index in 2019 barely satisfied the criterion for El Niño (Figure S1 in Supporting Information S1). Hence the 2019 extreme pIOD event is a unique case that allows for the separation of the impact of the pIOD on the terrestrial carbon cycle from other atmospheric modes affecting the IORC in the carbon satellite era.

The impact of the IOD on the terrestrial carbon cycle is not well understood compared with the intensive studies of the ENSO-related terrestrial carbon dynamics (Bastos et al., 2018; Kim et al., 2017; Liu et al., 2017; Wang et al., 2016; Wang, Zeng, Wang, Jiang, Wang, & Jiang, 2018; Wang, Zeng, Wang, Jiang, Chen, et al., 2018; Zeng et al., 2005). A limited number of studies (Wang et al., 2021; Williams & Hanan, 2011) based on model-simulated and satellite-derived gross primary productivity (GPP) have shown that the IOD could cause large anomalies in land photosynthesis over the IORC. Importantly, although uncertainties exist in future multimodel projections, extreme pIOD events are projected to become more frequent with global warming (Cai et al., 2014, 2020; Wang et al., 2021). Stronger modulations of the IOD on variations in GPP are suggested with increases in the explained variance by up to 10% over central and eastern Africa, Sumatra, and western and southeastern Australia in the future based on future projections of 10 Earth System Models (Wang et al., 2021).

Here, we investigated the impact of the extreme pIOD in 2019 on terrestrial net biome productivity (NBP) and its constituent fluxes over the IORC, based on the posterior fluxes optimized by the Global Carbon Assimilation System Version 2 (GCASv2) (Jiang et al., 2022, 2021), simulations from twelve state-of-the-art Terrestrial Biosphere Models (TBMs) that participated in the TRENDYv9 multimodel intercomparison (Sitch et al., 2015), two satellite-derived global GPP products, and the relevant climate data sets.

## 2. Materials and Methods

### 2.1. Global Carbon Assimilation System Version 2 (GCASv2)

GCASv2, an updated version of GCASv1, has the ability to assimilate the satellite-observed $XCO_2$. Its structure, implementation, and differences from GCASv1 have previously been described in detail (Jiang et al., 2021). GCASv2 adopted the assimilation technique of the ensemble square root filter (EnSRF) algorithm (Whitaker & Hamill, 2002) to assimilate the GOSAT ACOS $XCO_2$ version 9.0 Level 2 Lite product (O'Dell et al., 2012) within a 1-week window and generated the posterior results (both land and ocean fluxes) at $1° \times 1°$ with prescribed carbon emissions induced by fossil fuel and wildfires from 2010 to 2019 (Jiang et al., 2022). The transport model in GCASv2 is the Model for Ozone and Related chemical Tracers, version 4 (MOZART-4) (Emmons et al., 2010). It was driven by the GEOS-5 meteorological fields with a horizontal resolution of $1.9° \times 2.51°$ and 56 vertical layers. The prior surface carbon fluxes include (a) fossil fuel carbon emissions, which were calculated as the average of the Carbon Dioxide Information Analysis Center product (Andres et al., 2011) and the Open-source Data Inventory of Anthropogenic $CO_2$ emission product (Oda et al., 2018); (b) ocean carbon fluxes, which were from the $pCO_2$-Clim prior of CT2019B derived from the climatology of seawater pCO2 (Takahashi et al., 2009); (c) land carbon fluxes (net ecosystem exchange [NEE]), which were simulated by using the Boreal

Ecosystem Productivity Simulator (Chen et al., 1999), a process-based and remote sensing data-driven ecosystem model; and (d) wildfire carbon emissions, which were from the Global Fire Emissions Database version 4.1 (GFEDv4) (van der Werf et al., 2017). For this study, we performed additional validations at several surface flask sites across the study regions, showing the good performance of GCASv2 (Table S1 and Figure S2 in Supporting Information S1), and made a comparison with the ensemble NBP anomalies from OCO-2 v10 MIP LNLG experiment (Byrne et al., 2022) in September–December (SOND) 2019, showing that except over the Indo-China peninsula, they have basically consistent anomalous NBP patterns and comparable magnitudes over other regions of the IORC (Text S1 and Figure S3 in Supporting Information S1).

### 2.2. TRENDYv9 Simulations

We analyzed simulations from 12 state-of-the-art TBMs involved in the TRENDYv9 experiment, excluding some models that did not provide the relevant variables and three models (CLM5.0, SDGVM, and VISIT) whose NBP anomalies in SOND 2019 showed the lowest pattern correlation coefficients with the multimodel ensemble result over the IORC. Models in this study include CABLE-POP (Haverd et al., 2018), CLASSIC (Melton et al., 2020), IBIS (Yuan et al., 2014), ISAM (Meiyappan et al., 2015), ISBA-CTRIP (Delire et al., 2020), LPJ (Poulter et al., 2011), LPX-Bern (Lienert & Joos, 2018), OCN (Zaehle & Friend, 2010), ORCHIDEE (Krinner et al., 2005), ORCHIDEE-CNP (Goll et al., 2017), ORCHIDEEv3 (Vuichard et al., 2019), and YIBs (Yue & Unger, 2015) (Table S2 in Supporting Information S1). More detailed descriptions of these models have been provided in a previous study (Friedlingstein et al., 2020). The same experimental protocol was followed by these models in the TRENDY project, with the S3 run used here. In the S3 run, all the time-varying drivers—including the global atmospheric $CO_2$, climate, land use, gridded atmospheric N deposition, and N fertilizers—were taken into account to force the models (Sitch et al., 2015). In this study, the relevant variables were consistently interpolated into a horizontal resolution of $1° \times 1°$ by using the first-order conservative remapping scheme (Jones, 1999).

### 2.3. GOSAT Level 3 $XCO_2$ Product

The GOSAT Level 3 global $CO_2$ distribution product version 02.90 (O'Dell et al., 2012) was used in this study to infer the atmospheric $XCO_2$ anomalies related to the surface anomalous carbon fluxes. The FTS SWIR Level 3 $CO_2$ product was constructed by interpolating, extrapolating, and smoothing the FTS SWIR Level 2 column-averaged mixing ratios of $CO_2$ with the kriging method on a monthly basis. This product has a time period starting from June 2009 and a horizontal resolution of $2.5° \times 2.5°$.

### 2.4. Satellite-Derived GPP Products

We adopted two satellite-based global terrestrial GPP products to decompose the posterior NBP into its constituent fluxes in the carbon assimilation system: the GOSIF GPP (Li & Xiao, 2019b) and FluxSat GPP (Joiner et al., 2018). We used their average and standard deviation to represent the GPP anomalies and uncertainties induced by the pIOD in 2019 over the India-Africa and Asia-Pacific regions.

The GOSIF GPP product was generated based on the global, fine-resolution Orbiting Carbon Observatory-2 (OCO-2)-based SIF product (GOSIF) (Li & Xiao, 2019a) and linear relationships between solar-induced fluorescence (SIF) and GPP across a wide variety of biomes at both site and grid cell levels. The GOSIF product is provided at 0.05° and each 8 days across the globe from 2000 to 2020. The FluxSat version 1 GPP product was generated by using satellite-based geometry-adjusted reflectances from the MODIS and SIF from the Global Ozone Monitoring Experiment 2 (GOME-2) within a simplified light-use efficiency framework without any meteorological inputs. The monthly FluxSat GPP product used here had a 0.5° spatial resolution since 2000.

### 2.5. Climate Data Sets

Land precipitation and surface air temperature were obtained from the version 4.05 of the Climatic Research Unit (CRU) Time Series (TS) monthly high-resolution gridded data set at 0.5° spatial resolution (Harris et al., 2020). The root zone soil moisture was from the NASA's Global Land Data Assimilation System (GLDAS) Noah land Surface Model L4 monthly V2.1 data set (GLDAS_NOAH025_M) at 0.25° spatial resolution (Rodell et al., 2004). And the root depth in Noah depends on the vegetation types. The SST and U and V winds at 50 and 200 hPa were

adopted from the ERA5 reanalysis data set (Hersbach et al., 2020). The ERA5 data set was produced by using 4D-Var data assimilation and model forecasts in CY41R2 of the ECMWF Integrated Forecast System, with 137 hybrid sigma/pressure levels in the vertical and 31 km horizontal resolution.

### 2.6. Velocity Potential and Divergent Winds

To investigate the climate extremes-related atmospheric circulation adjustments caused by the extreme pIOD in 2019, we here adopted the concepts of velocity potential and divergent winds at 200 hPa to illustrate the atmospheric vertical motion and divergence, following the previous analysis (Wang et al., 2021). According to the Helmholtz theorem, the horizontal velocity vector ($\vec{v}$) can be decomposed into irrotational ($\vec{v}_\chi$, divergent winds) and nondivergent ($\vec{v}_\psi$) parts:

$$\vec{v} = \vec{v}_\chi + \vec{v}_\psi = \nabla_H \chi + \vec{k} \times \nabla_H \psi, \tag{1}$$

where $\chi$ is the velocity potential, $\psi$ is the stream function, and $\nabla_H$ is the horizontal vector differential operator. The $\vec{k}$ represents the unit vector directed vertically. Taking the divergence of Equation 1, we can obtain the following equation:

$$\nabla^2 \chi = \nabla \cdot \vec{v} = \text{Div}, \tag{2}$$

where Div is the horizontal divergence. Solving this Poisson's equation, we can derive the velocity potential and then the divergent winds.

### 2.7. Anomaly Calculation

As a result of the short-term period (10 years) of the posterior results from GCASv2, we derived the anomalies of all the carbon fluxes by removing their climatology calculated from 2010 to 2019. For the GOSAT L3 $XCO_2$ product, we first detrended the monthly $XCO_2$ at each grid, which is largely caused by anthropogenic fossil fuel emissions, simply by removing the corresponding zonal average. We then calculated the $XCO_2$ anomalies used in this study by removing their climatology calculated from 2010 to 2019.

## 3. Results and Discussion

### 3.1. Pattern of NBP Anomalies Induced by the 2019 Extreme pIOD Associated With Its Climate Drivers

The posterior NBP anomalies averaged from SOND 2019 in GCASv2 showed contrasting behaviors over the IORC, exhibiting enhanced carbon uptake (positive values) over western, eastern, and central Africa and India, but enhanced carbon release (negative values) over southern Africa, East Asia, the Indo-China peninsula, Indonesia, and Australia (Figure 1a). TRENDYv9 multimodel ensemble NBP anomalies suggested a similar spatial pattern, although the magnitudes differed in some regions (Figures 1a and 1b). For instance, the enhanced carbon uptake indicated by the TRENDYv9 ensemble NBP was weaker than the GCASv2 NBP over eastern Africa but was stronger over India (Figures 1a and 1b). However, patterns of NBP anomalies in TBMs showed a large intermodel spread (Figure S4 in Supporting Information S1) despite following the same experimental protocol, likely caused by differences in model structures and parameters (Rogers et al., 2014; Sitch et al., 2015).

From the perspective of atmospheric $CO_2$ concentration, persistent anomalies in surface carbon sources and sinks can result in regional atmospheric $CO_2$ concentration anomalies. Satellite-observed $XCO_2$ concentrations can directly detect anomalies in terrestrial carbon fluxes in local or upwind regions to some extent (Figure 1c), despite the interference from atmospheric advection and divergence. Obvious reductions in the GOSAT L3 $XCO_2$ anomalies occurred over the vast areas to the north of Lake Victoria in Africa (Figure 1c), which corresponded well with enhanced terrestrial carbon uptake in this region associated with the prevailing southeasterly winds in the lower troposphere (Figure 1a). By contrast, there were clear increases in the $XCO_2$ anomalies over East Asia, the
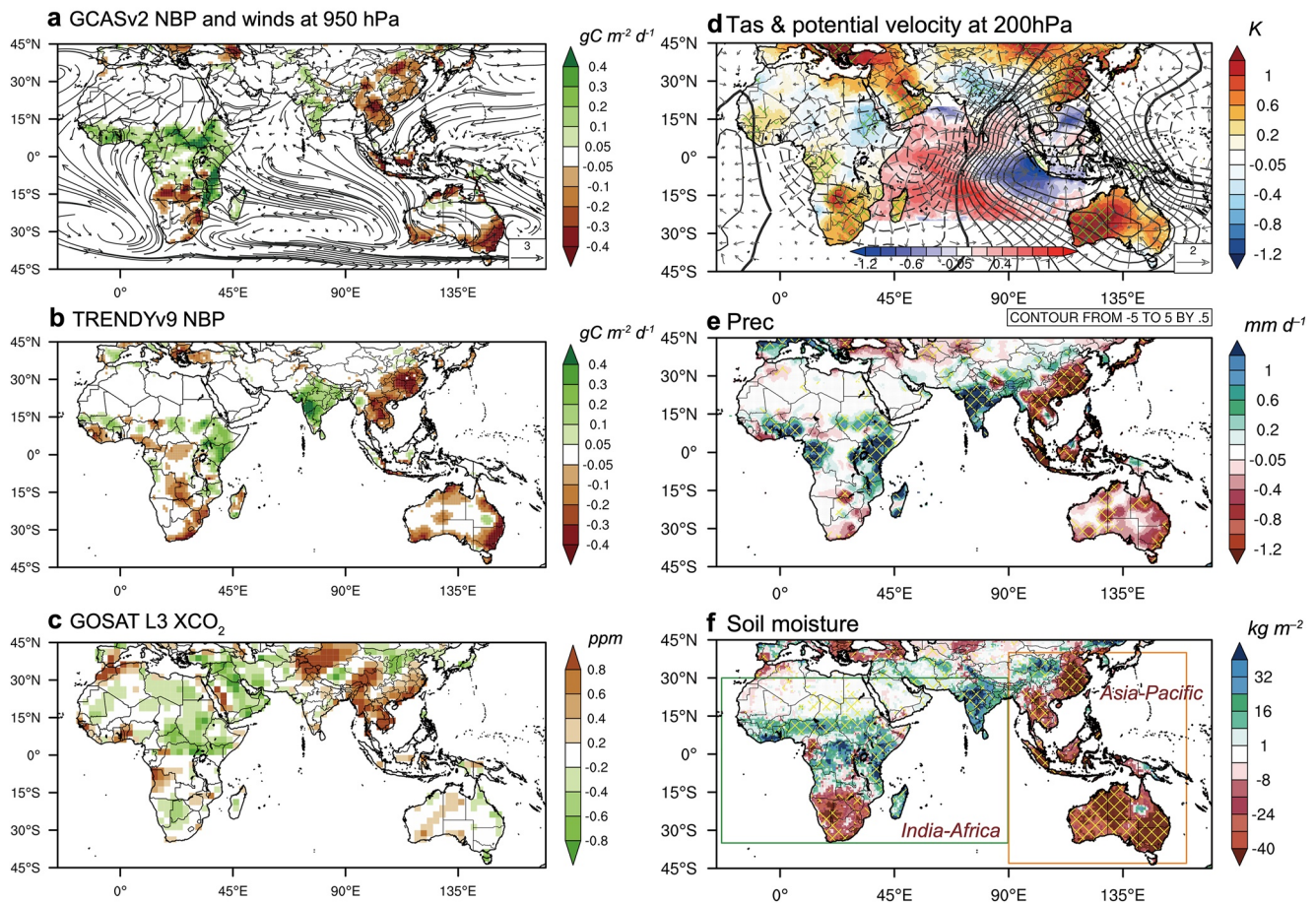
**Figure 1.** Patterns of terrestrial carbon flux, atmospheric XCO$_2$, and climate anomalies averaged from September to December (SOND) 2019. (a) Posterior net biome productivity (NBP; positive indicates a flux from the atmosphere to the land) optimized by the Global Carbon Assimilation System Version 2.0 (GCASv2) and winds at 950 hPa (arrows). (b) Ensemble NBP anomalies simulated with multiple models involved in TRENDYv9. The units of NBP and winds in (a and b) are gC m$^{-2}$ d$^{-1}$ and m s$^{-1}$, respectively. (c) GOSAT L3 XCO$_2$ anomalies over lands in ppm. (d) Surface air temperature anomalies and sea surface temperature over the tropical Indian Ocean (k) associated with the anomalies of velocity potential (contours) and divergent winds at 200 hPa (arrows) with respective units of 10$^6$ m$^2$ s$^{-1}$ and m s$^{-1}$. (e) Precipitation anomalies (mm d$^{-1}$). (f) Global Land Data Assimilation System root zone soil moisture anomalies (kg m$^{-2}$). The green and orange boxes in (f) represent the two land regions of India-Africa and Asia-Pacific used to calculate the total terrestrial carbon fluxes and anomalies. The cross-hatched areas represent variations in SOND stronger than ±1−σ during the time period of 2010–2019.

Indo-China peninsula, Sumatra, Kalimantan Island, and western parts of Australia (Figure 1c), and the increases in XCO$_2$ anomalies in these regions were consistent with the enhancement of carbon release (Figure 1a).

These NBP anomalies over the IORC can be largely accounted for by the anomalous weather and climate induced by the extreme pIOD in 2019. The warm pole of the extreme pIOD over the equatorial western Indian Ocean favored active convection (Figure 1d), resulting in high precipitation over western, eastern, and central Africa and India (Figure 1e). More precipitation led to a wetter land surface (Figure 1f), more evapotranspiration, and thus more evaporative cooling and lower near-surface air temperature (Figure 1d) as a result of the control of thermodynamics and the hydrological cycle on the surface energy balance over the tropics (Zeng & Neelin, 1999). The cool and wet conditions enhanced terrestrial carbon uptake over these regions (Figures 1a and 1b) likely due to strengthened terrestrial photosynthesis (Wang et al., 2021; Zeng et al., 2005; Zscheischler et al., 2014), reduced soil respiration, and inhibition of wildfires (Kim et al., 2019). By contrast, atmospheric subsidence prevailed over East Asia, the Indo-China peninsula, Indonesia, and Australia due to the cold pole of the pIOD over the southeastern equatorial Indian Ocean (Figure 1d). This caused a reduction in precipitation (Figure 1e), higher temperatures (Figure 1d), and thus widespread heatwaves and droughts (Figures 1d and 1f). These climate extremes, a multivariate compound event, can potentially reduce photosynthesis by stomatal and xylem

regulation (Bastos et al., 2021; Konings et al., 2017; Peters et al., 2018; Wang et al., 2021), increase vegetation mortality (Senf et al., 2020; Stovall et al., 2019), increase soil respiration (Anjileli et al., 2021), and promote wild-fires (Boer et al., 2020; Wang et al., 2020), hence enhancing anomalous carbon release there (Figures 1a and 1b).

In the developing phase of the pIOD during June–August (JJA) 2019 (Figure S5c in Supporting Information S1), the enhanced convection and subsidence associated with the pIOD were weaker than those during SOND 2019 (pIOD peaked in October) (Figure 1d). Nevertheless, it had already to some extent enhanced precipitation over Africa north of the Equator and India, and reduced precipitation over southern China, the Indo-China peninsula, Sumatra, Kalimantan Island, and southeastern Australia (Figure S5d in Supporting Information S1). Compared to the precipitation pattern in March–May (MAM) 2019, which was largely influenced by the weak El Niño event in 2018 (Figure S5b in Supporting Information S1), these changes in precipitation in JJA 2019 indicate the gradual transition from the control of El Niño to the control of pIOD, which also manifested in changes of NBP. Increased carbon uptake over the Africa north of the Equator and western coast of India could be found in both of the GCASv2 and TRENDYv9 ensemble result (Figures S6c and S6d in Supporting Information S1). An obvious carbon release was found over southern China in JJA (Figures S6c and S6d in Supporting Information S1) which was associated with decreased precipitation (Figure S5d in Supporting Information S1), differing from the weak uptake there in MAM (Figure S6b in Supporting Information S1) caused by the El Niño-induced more precipitation (Figure S5b in Supporting Information S1). Additionally, there was an obvious reduction in carbon release over Australia from MAM to JJA (Figure S6 in Supporting Information S1). These changes in NBP anomalies from MAM to JJA make us more confident that NBP anomalies in SOND 2019 focused in this study were mainly induced by the extreme pIOD event (Figures 1a and 1b).

### 3.2. Seasonal Variations of Total Regional NBP Anomalies

Given that the 2019 extreme pIOD had differential impacts on the terrestrial carbon sources and sinks over the IORC (Figures 1a and 1b), we simply separated these regions into two parts: the India-Africa and Asia-Pacific regions (Figure 1f).

Over the India-Africa region, the seasonal variation in GCASv2 NBP showed net carbon uptake from August to October and net carbon release in other months (Figure 2a). In 2019, the anomalous carbon release relative to the average from 2010 to 2019 occurred before August, followed by the anomalous carbon uptake, with the averaged anomalies of $-0.06 \pm 0.15$ PgC in JJA and $0.23 \pm 0.20$ PgC in SOND (Figure 2a). The TRENDYv9 ensemble showed carbon uptake from June to October and carbon release in other months (Figure 2c), which was somewhat different from the GCASv2 (Figure 2a). The anomalies in 2019 ($0.02 \pm 0.07$ PgC in JJA and $0.11 \pm 0.15$ PgC in SOND) based on TRENDYv9 were slightly weaker than those in GCASv2 (Figures 2a and 2c). These positive anomalies in the total NBP in SOND were linked to the enhanced carbon uptake over western, eastern, and central Africa and India (Figures 1a and 1c). The 2015 extreme El Niño caused anomalous carbon release in the tropics with no obvious lagged response (Bastos et al., 2018; Liu et al., 2017; Wang, Zeng, Wang, Jiang, Wang, & Jiang, 2018). By comparison, in 2015, GCASv2 showed nearly neutral anomalies ($-0.01 \pm 0.15$ PgC) in JJA and obvious carbon release ($-0.28 \pm 0.19$ PgC) in SOND (Figure 2a), and the TRENDYv9 ensemble indicated carbon release of $-0.11 \pm 0.09$ PgC in JJA and $-0.14 \pm 0.11$ PgC in SOND (Figure 2c). Both products showed the comparable magnitudes but different signs of carbon anomalies in SOND induced by the 2019 extreme pIOD and 2015 extreme El Niño events (Figures 2a and 2c), which can be clearly seen from their different spatial patterns of NBP and climate anomalies in these two events (Figure 1 and Figures S7 and S8 in Supporting Information S1). It suggests that, in addition to ENSO events, IOD events can also play an important part in influencing regional carbon cycling.

Over the Asia-Pacific region, GCASv2 and TRENDYv9 showed similar seasonal variations in NBP and both showed net carbon uptake from April to October, although the magnitudes differed (Figures 2b and 2d). Carbon anomalies in 2019 showed enhanced carbon release in all months, which was consecutively influenced by the lagged effects (Wang et al., 2016) of the weak El Niño in 2018 and the extreme pIOD in 2019 (Figures S1 and S6 in Supporting Information S1). The anomalous carbon release was $-0.18 \pm 0.12$ PgC in JJA and $-0.38 \pm 0.15$ PgC in SOND in GCASv2, and $-0.08 \pm 0.08$ PgC in JJA and $-0.23 \pm 0.20$ PgC in SOND in the TRENDYv9 ensemble, respectively (Figures 2b and 2d). By comparison, the 2015 extreme El Niño event also caused anomalous carbon release in SOND (somewhat weaker than those in 2019), with anomalies of $-0.28 \pm 0.16$ PgC in GCASv2 and $-0.18 \pm 0.12$ PgC in the TRENDYv9 ensemble, respectively (Figures 2b and 2d).
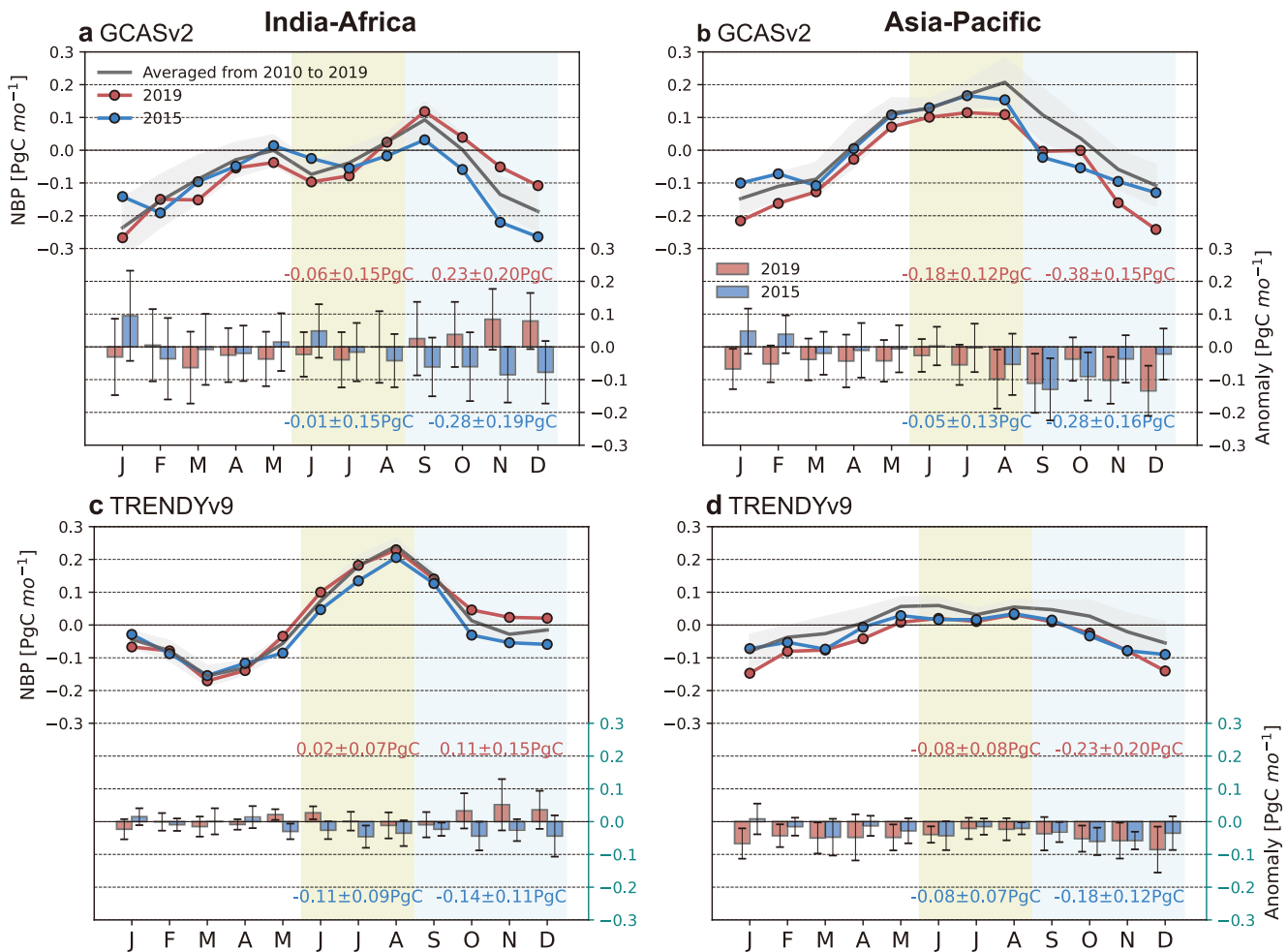
**Figure 2.** Seasonal variations in total net biome productivity (NBP) and its anomalies over the India-Africa and Asia-Pacific regions. The posterior total NBP anomalies in 2015 and 2019 optimized by Global Carbon Assimilation System for the (a) India-Africa and (b) Asia-Pacific regions. The error bars in (a and b) are the uncertainties calculated from the optimization process. The TRENDYv9 ensemble NBP in 2015 and 2019 for the (c) India-Africa and (d) Asia-Pacific regions. The error bars in (c and d) represent the standard deviation among different models. The light gray shaded areas represent the standard deviation of the NBP for each month from 2010 to 2019. The light orange and blue shaded areas in the subplots represent June–August and September–December.

In addition, the historical variations in the NBP during SOND, in general, had stronger partial correlation coefficients (*pcor*) with the root zone soil moisture (controlling the effect of temperature) than with temperature (controlling the effect of soil moisture) for both the India-Africa and Asia-Pacific regions, except that the TRENDYv9 ensemble had equivalent *pcor* with the root zone soil moisture and temperature over the India-Africa region (Table S3 in Supporting Information S1). This indicates that soil moisture played a more important role in these regional NBP variations, in agreement with the findings of previous studies (Humphrey et al., 2018; Humphrey et al., 2021; Wang, Zeng, Wang, Jiang, Chen, et al., 2018; Zscheischler et al., 2014), as would also be expected in tropical regions.

### 3.3. Biological Mechanisms

The carbon balance over land is represented by NBP = NEP − $D$ = GPP − TER − $D$, where NEP denotes net ecosystem productivity, $D$ is the carbon release induced by both natural and anthropogenic disturbances such as wildfires, harvests, grazing, and land cover change, and TER is the total ecosystem respiration. We decomposed NBP anomalies during SOND in 2019 into its different constituent fluxes. In GCASv2, we optimized the terrestrial NEE or −NEP and ocean carbon flux using satellite $CO_2$ column data, while $D$ mainly represents the prescribed carbon emission induced by wildfires. In this study, we used the average of GOSIF GPP (Li &
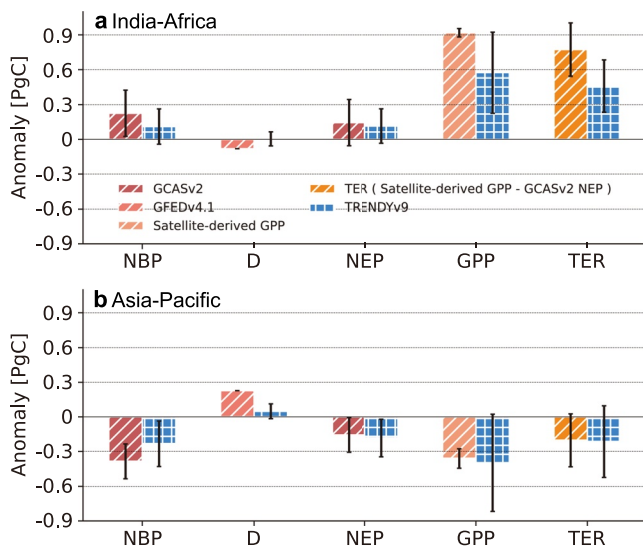
**Figure 3.** Anomalies in the net biome productivity (NBP) and its constituent fluxes during September–December 2019. (a) Terrestrial carbon fluxes over the India-Africa region. (b) Terrestrial carbon fluxes over the Asia-Pacific region. The constituent fluxes of the NBP in the TRENDYv9 ensemble were simulated with the intermodel spread (standard deviation among different models; error bars). The term $D$ is the residual between simulated net ecosystem productivity (NEP) and NBP, which includes fluxes of simulated wildfires, grazing, harvest etc. In GCASv2, the uncertainties in the NBP and NEP (error bars) are calculated from the optimization process. $D$ is only composed of the fluxes of wildfires based on the Global Fire Emissions Database without uncertainties, we supposed. The gross primary productivity (GPP) is the average of the GOSIF GPP and FluxSat GPP with their standard deviation as uncertainties. The total ecosystem respiration is calculated as the difference between the satellite-derived GPP and the GCASv2 optimized NEP.

Xiao, 2019b) and FluxSat GPP (Joiner et al., 2018), two satellite-based GPP products, to calculate the GPP anomalies. TER is therefore derived as the difference between the satellite-derived GPP and optimized NEP.

Over the India-Africa region (Figure 3a), the enhanced NEP ($0.14 \pm 0.20$ Pg C) accounted for 60.87% of the enhanced NBP ($0.23 \pm 0.20$ Pg C) in GCASv2 induced by the wet and cool conditions during SOND (Figures 1d–1f). The increase in the NEP resulted from the stronger enhancement in the GPP ($0.92 \pm 0.04$ PgC) than in the TER ($0.77 \pm 0.23$ PgC). In the TRENDYv9 ensemble results, the enhanced NEP ($0.12 \pm 0.15$ PgC) accounted for 103.97% of the variation in the NBP, with the enhancement in the NEP similarly caused by the stronger enhancement in the GPP ($0.57 \pm 0.35$ Pg C) than in the TER ($0.46 \pm 0.22$ PgC).

Over the Asia-Pacific region (Figure 3b), the anomalies in the $D$ and NEP accounted for 59.17% and 40.83% of the reduced NBP ($-0.38 \pm 0.15$ PgC) in GCASv2 caused by the dry and heat compounds (Figures 1d–1f), respectively. A stronger reduction in the GPP ($-0.36 \pm 0.08$ PgC) than in the TER ($-0.20 \pm 0.23$ PgC) appeared to cause the reduction in the NEP. The reduction in the NEP estimated by the TRENDYv9 ensemble ($-0.18 \pm 0.16$ PgC) was comparable with the magnitude in GCASv2, but the reduction in the NEP accounted for a much larger fraction of the variation of the NBP in the TRENDYv9 ensemble (79.18%) than in GCASv2. The anomalies in the GPP ($-0.40 \pm 0.42$ PgC) and TER ($-0.21 \pm 0.31$ PgC) in the TRENDYv9 ensemble had comparable magnitudes to the estimates in the satellite-derived GPP and calculated TER.

Quantitatively, the GPP had the largest variations among these three processes (GPP, TER, and D) over both of India-Africa and Asia-Pacific regions and dominated the enhanced terrestrial carbon uptake and release over the India-Africa and Asia-Pacific regions, respectively (Figure 3). The reductions in the GPP and TER simulated in the TRENDYv9 ensemble had large intermodel spreads due to their different model structures and parameters; their individual estimates are illustrated in Tables S4 and S5 in Supporting Information S1. Furthermore, the carbon flux anomaly mainly induced by wildfires ($D$) was substantially underestimated in the TRENDYv9 ensemble results (Figure 3). We found that this substantial underestimation in $D$ anomalies still existed although we derived the magnitude by only using the models that explicitly included the fire modules (Tables S2, S4, and S5 in Supporting Information S1). This indicated that the underestimation in $D$ anomalies was largely caused by the absence and underrepresentation of wildfire in the models (Table S2 in Supporting Information S1). If the magnitudes of the wildfire-induced carbon anomalies simulated by the TRENDYv9 ensemble were close to the magnitudes derived from satellites (van der Werf et al., 2017), as used in GCASv2, then the magnitudes of the total NBP anomalies over the two regions would have been comparable between GCASv2 and the TRENDYv9 ensemble (Figure 3).

## 4. Conclusions

We in this study comprehensively investigated the impact of the 2019 extreme pIOD on terrestrial NBP and its constituent fluxes, and quantitatively compared it with the impact of the 2015 extreme El Niño during SOND. GCASv2 posterior NBP and TRENDYv9 multimodel ensemble NBP anomalies basically showed similar pIOD-induced spatial patterns, exhibiting enhanced carbon uptake over western, eastern, and central Africa and India, but enhanced carbon release over southern Africa, East Asia, the Indo-China peninsula, Indonesia, and Australia. It caused an enhanced total terrestrial carbon uptake of $0.23 \pm 0.20$ PgC in GCASv2 and $0.11 \pm 0.15$ PgC in TRENDYv9 ensemble over the India-Africa region, and the enhanced total release of $0.38 \pm 0.15$ PgC in GCASv2 and $0.23 \pm 0.20$ PgC in TRENDYv9 ensemble over the Asia-Pacific region, respectively. We further revealed that these regional NBP anomalies were more closely related to soil water availability with a dominant role of GPP. Importantly, these two data sets showed comparable magnitudes to those following

the 2015 extreme El Niño event although this event led to the consistent release of carbon in both India-Africa and Asia-Pacific regions. This suggests that, other than ENSO events, IOD events can also drive variations in the regional terrestrial carbon cycling. Along with more frequent extreme pIOD events in future greenhouse warming, it may also modulate the long-term land carbon accumulations (Cai et al., 2014; Park et al., 2020).

## Data Availability Statement

Land precipitation and surface air temperature from CRU TS v. 4.05 are available at https://crudata.uea.ac.uk/cru/data/hrg/. GLDAS-2.1 soil moisture is maintained at the NASA Goddard Earth Science Data and Information Services Center (GES DISC) with the web site at https://disc.gsfc.nasa.gov/datasets. Winds at 950 and 200 hPa from ERA5 are available at https://cds.climate.copernicus.eu/cdsapp#!/dataset/reanalysis-era5-pressure-levels-monthly-means?tab=form. GOSIF GPP and FluxSat GPP products are provided at https://globalecology.unh.edu/data/GOSIF-GPP.html and https://avdc.gsfc.nasa.gov/pub/tmp/FluxSat_GPP/, respectively. The TRENDY DGVMs data are available at https://sites.exeter.ac.uk/trendy. GCASv2 output are available at https://zenodo.org/record/5829774.

## References

Andres, R. J., Gregg, J. S., Losey, L., Marland, G., & Boden, T. A. (2011). Monthly, global emissions of carbon dioxide from fossil fuel consumption. *Tellus B: Chemical and Physical Meteorology*, *63*(3), 309–327. https://doi.org/10.3402/tellusb.v63i3.16211

Anjileli, H., Huning, L. S., Moftakhari, H., Ashraf, S., Asanjan, A. A., Norouzi, H., & AghaKouchak, A. (2021). Extreme heat events heighten soil respiration. *Scientific Reports*, *11*(1), 6632. https://doi.org/10.1038/s41598-021-85764-8

Ashok, K., Guan, Z., & Yamagata, T. (2003). Influence of the Indian Ocean Dipole on the Australian winter rainfall. *Geophysical Research Letters*, *30*(15), 1821. https://doi.org/10.1029/2003gl017926

Ashok, K., Guan, Z. Y., Saji, N. H., & Yamagata, T. (2004). Individual and combined influences of ENSO and the Indian Ocean Dipole on the Indian summer monsoon. *Journal of Climate*, *17*(16), 3141–3155. https://doi.org/10.1175/1520-0442(2004)017<3141:iacioe>2.0.co;2

Bastos, A., Friedlingstein, P., Stephen, S., Bastos, A., Chen, C., Mialon, A., et al. (2018). Impact of the 2015/2016 El Niño on the terrestrial carbon cycle constrained by bottom-up and top-down approaches. *Philosophical Transactions of the Royal Society of London. Series B, Biological sciences*, *373*(1760), 20170304.

Bastos, A., Orth, R., Reichstein, M., Ciais, P., Viovy, N., Zaehle, S., et al. (2021). Vulnerability of European ecosystems to two compound dry and hot summers in 2018 and 2019. *Earth System Dynamics*, *12*(4), 1015–1035. https://doi.org/10.5194/esd-12-1015-2021

Behera, S. K., Luo, J. J., Masson, S., Delecluse, P., Gualdi, S., Navarra, A., & Yamada, T. (2005). Paramount impact of the Indian Ocean Dipole on the East African short rains: A CGCM Study. *Journal of Climate*, *18*(21), 4514–4530. https://doi.org/10.1175/jcli3541.1

Behera, S. K., Luo, J. J., Masson, S., Rao, S. A., Sakuma, H., & Yamagata, T. (2006). A CGCM Study on the interaction between IOD and ENSO. *Journal of Climate*, *19*(9), 1688–1705. https://doi.org/10.1175/jcli3797.1

Boer, M. M., Resco de Dios, V., & Bradstock, R. A. (2020). Unprecedented burn area of Australian mega forest fires. *Nature Climate Change*, *10*(3), 171–172. https://doi.org/10.1038/s41558-020-0716-1

Byrne, B., Baker, D. F., Basu, S., Bertolacci, M., Bownam, K. W., Carroll, D., et al. (2022). National $CO_2$ budgets (2015–2020) inferred from atmospheric $CO_2$ observations in support of the Global Stocktake. *Earth System Science Data Discussions*, *2022*, 1–59.

Byrne, B., Liu, J., Lee, M., Yin, Y., Bowman, K. W., Miyazaki, K., et al. (2021). The carbon cycle of Southeast Australia during 2019–2020: Drought, fires, and subsequent recovery. *AGU Advances*, *2*(4), e2021AV000469. https://doi.org/10.1029/2021av000469

Cai, W., Cowan, T., & Raupach, M. (2009). Positive Indian Ocean Dipole events precondition southeast Australia bushfires. *Geophysical Research Letters*, *36*(19), L19710. https://doi.org/10.1029/2009gl039902

Cai, W., Santoso, A., Wang, G., Weller, E., Wu, L., Ashok, K., et al. (2014). Increased frequency of extreme Indian Ocean Dipole events due to greenhouse warming. *Nature*, *510*(7504), 254–258. https://doi.org/10.1038/nature13327

Cai, W., van Rensch, P., Cowan, T., & Hendon, H. H. (2011). Teleconnection pathways of ENSO and the IOD and the mechanisms for impacts on Australian rainfall. *Journal of Climate*, *24*(15), 3910–3923. https://doi.org/10.1175/2011jcli4129.1

Cai, W., Yang, K., Wu, L., Huang, G., Santoso, A., Ng, B., et al. (2020). Opposite response of strong and moderate positive Indian Ocean Dipole to global warming. *Nature Climate Change*, *11*(1), 27–32. https://doi.org/10.1038/s41558-020-00943-1

Chen, J. M., Liu, J., Cihlar, J., & Goulden, M. L. (1999). Daily canopy photosynthesis model through temporal and spatial scaling for remote sensing applications. *Ecological Modelling*, *124*(2–3), 99–119. https://doi.org/10.1016/s0304-3800(99)00156-8

Delire, C., Seferian, R., Decharme, B., Alkama, R., Calvet, J., Carrer, D., et al. (2020). The global land carbon cycle simulated with ISBA-CTRIP: Improvements over the last decade. *Journal of Advances in Modeling Earth Systems*, *12*(9), e2019MS001886. https://doi.org/10.1029/2019ms001886

Emmons, L. K., Walters, S., Hess, P. G., Lamarque, J. F., Pfister, G. G., Fillmore, D., et al. (2010). Description and evaluation of the model for Ozone and Related Chemical Tracers, Version 4 (MOZART-4). *Geoscientific Model Development*, *3*(1), 43–67. https://doi.org/10.5194/gmd-3-43-2010

Friedlingstein, P., O'Sullivan, M., Jones, M. W., Andrew, R. M., Hauck, J., Olsen, A., et al. (2020). Global carbon budget 2020. *Earth System Science Data*, *12*(4), 3269–3340.

Goll, D. S., Winkler, A. J., Raddatz, T., Dong, N., Prentice, I. C., Ciais, P., & Brovkin, V. (2017). Carbon-nitrogen interactions in idealized simulations with JSBACH (version 3.10). *Geoscientific Model Development*, *10*(5), 2009–2030. https://doi.org/10.5194/gmd-10-2009-2017

Harris, I., Osborn, T. J., Jones, P., & Lister, D. (2020). Version 4 of the CRU TS monthly high-resolution gridded multivariate climate dataset. *Scientific Data*, *7*(1), 109. https://doi.org/10.1038/s41597-020-0453-3

Haverd, V., Smith, B., Nieradzik, L., Briggs, P. R., Woodgate, W., Trudinger, C. M., et al. (2018). A new version of the CABLE land surface model (Subversion revision r4601) incorporating land use and land cover change, woody vegetation demography, and a novel optimisation-based

approach to plant coordination of photosynthesis. *Geoscientific Model Development*, *11*(7), 2995–3026. https://doi.org/10.5194/gmd-11-2995-2018

Hersbach, H., Bell, B., Berrisford, P., Hirahara, S., Horanyi, A., Munoz-Sabater, J., et al. (2020). The ERA5 global reanalysis. *Quarterly Journal of the Royal Meteorological Society*, *146*(730), 1999–2049. https://doi.org/10.1002/qj.3803

Humphrey, V., Berg, A., Ciais, P., Gentine, P., Jung, M., Reichstein, M., et al. (2021). Soil moisture–atmosphere feedback dominates land carbon uptake variability. *Nature*, *592*(7852), 65–69. https://doi.org/10.1038/s41586-021-03325-5

Humphrey, V., Zscheischler, J., Ciais, P., Gudmundsson, L., Sitch, S., & Seneviratne, S. I. (2018). Sensitivity of atmospheric $CO_2$ growth rate to observed changes in terrestrial water storage. *Nature*, *560*(7720), 628–631. https://doi.org/10.1038/s41586-018-0424-4

Jiang, F., Ju, W., He, W., Wu, M., Wang, H., Wang, J., et al. (2022). A 10-year global monthly averaged terrestrial net ecosystem exchange dataset inferred from the ACOS GOSAT v9 XCO2 retrievals (GCAS2021). *Earth System Science Data*, *14*(7), 3013–3037. https://doi.org/10.5194/essd-14-3013-2022

Jiang, F., Wang, H., Chen, J. M., Ju, W., Tian, X., Feng, S., et al. (2021). Regional $CO_2$ fluxes from 2010 to 2015 inferred from GOSAT $XCO_2$ retrievals using a new version of the Global Carbon Assimilation System. *Atmospheric Chemistry and Physics*, *21*(3), 1963–1985. https://doi.org/10.5194/acp-21-1963-2021

Joiner, J., Yoshida, Y., Zhang, Y., Duveiller, G., Jung, M., Lyapustin, A., et al. (2018). Estimation of terrestrial global gross primary production (GPP) with satellite data-driven models and eddy covariance flux data. *Remote Sensing*, *10*(9), 1346. https://doi.org/10.3390/rs10091346

Jones, P. W. (1999). First- and second-order conservative remapping schemes for grids in spherical coordinates. *Monthly Weather Review*, *127*(9), 2204–2210. https://doi.org/10.1175/1520-0493(1999)127<2204:fasocr>2.0.co;2

Kim, J.-S., Jeong, S.-J., Kug, J.-S., & Williams, M. (2019). Role of local air-sea interaction in fire activity over equatorial Asia. *Geophysical Research Letters*, *46*(24), 14789–14797. https://doi.org/10.1029/2019gl085943

Kim, J.-S., Kug, J.-S., & Jeong, S.-J. (2017). Intensification of terrestrial carbon cycle related to El Niño–Southern Oscillation under greenhouse warming. *Nature Communications*, *8*(1), 1674. https://doi.org/10.1038/s41467-017-01831-7

Konings, A. G., Williams, A. P., & Gentine, P. (2017). Sensitivity of grassland productivity to aridity controlled by stomatal and xylem regulation. *Nature Geoscience*, *10*(4), 284–288. https://doi.org/10.1038/ngeo2903

Krinner, G., Viovy, N., de Noblet-Ducoudre, N., Ogee, J., Polcher, J., Friedlingstein, P., et al. (2005). A dynamic global vegetation model for studies of the coupled atmosphere-biosphere system. *Global Biogeochemical Cycles*, *19*(1), GB1015. https://doi.org/10.1029/2003gb002199

Li, X., & Xiao, J. (2019a). A global, 0.05-degree product of solar-induced chlorophyll fluorescence derived from OCO-2, MODIS, and reanalysis data. *Remote Sensing*, *11*(5), 517. https://doi.org/10.3390/rs11050517

Li, X., & Xiao, J. (2019b). Mapping photosynthesis solely from solar-induced chlorophyll fluorescence: A global, fine-resolution dataset of gross primary production derived from OCO-2. *Remote Sensing*, *11*(21), 2563. https://doi.org/10.3390/rs11212563

Lienert, S., & Joos, F. (2018). A Bayesian ensemble data assimilation to constrain model parameters and land-use carbon emissions. *Biogeosciences*, *15*(9), 2909–2930. https://doi.org/10.5194/bg-15-2909-2018

Liu, J., Bowman, K. W., Schimel, D. S., Parazoo, N. C., Jiang, Z., Lee, M., et al. (2017). Contrasting carbon cycle responses of the tropical continents to the 2015-2016 El Niño. *Science*, *358*(6360), eaam5690. https://doi.org/10.1126/science.aam5690

Meiyappan, P., Jain, A. K., & House, J. I. (2015). Increased influence of nitrogen limitation on $CO_2$ emissions from future land use and land use change. *Global Biogeochemical Cycles*, *29*(9), 1524–1548. https://doi.org/10.1002/2015gb005086

Melton, J. R., Arora, V. K., Wisernig-Cojoc, E., Seiler, C., Fortier, M., Chan, E., & Teckentrup, L. (2020). CLASSIC v1.0: The open-source community successor to the Canadian land surface scheme (CLASS) and the Canadian terrestrial ecosystem model (CTEM)—Part 1: Model framework and site-level performance. *Geoscientific Model Development*, *13*(6), 2825–2850. https://doi.org/10.5194/gmd-13-2825-2020

Oda, T., Maksyutov, S., & Andres, R. J. (2018). The open-source data inventory for anthropogenic $CO_2$, version 2016 (ODIAC2016): A global monthly fossil fuel $CO_2$ gridded emissions data product for tracer transport simulations and surface flux inversions. *Earth System Science Data*, *10*(1), 87–107. https://doi.org/10.5194/essd-10-87-2018

O'Dell, C. W., Connor, B., Bosch, H., O'Brien, D., Frankenberg, C., Castano, R., et al. (2012). The ACOS CO2 retrieval algorithm—Part 1: Description and validation against synthetic observations. *Atmospheric Measurement Techniques*, *5*(1), 99–121. https://doi.org/10.5194/amt-5-99-2012

Park, S. W., Kim, J. S., Kug, J. S., Stuecker, M. F., Kim, I. W., & Williams, M. (2020). Two Aspects of decadal ENSO variability modulating the long-term global carbon cycle. *Geophysical Research Letters*, *47*(8), e2019GL086390. https://doi.org/10.1029/2019gl086390

Peters, W., van der Velde, I. R., van Schaik, E., Miller, J. B., Ciais, P., Duarte, H. F., et al. (2018). Increased water-use efficiency and reduced $CO_2$ uptake by plants during droughts at a continental-scale. *Nature Geoscience*, *11*(9), 744–748. https://doi.org/10.1038/s41561-018-0212-7

Poulter, B., Frank, D. C., Hodson, E. L., & Zimmermann, N. E. (2011). Impacts of land cover and climate data selection on understanding terrestrial carbon dynamics and the $CO_2$ airborne fraction. *Biogeosciences*, *8*(8), 2027–2036. https://doi.org/10.5194/bg-8-2027-2011

Rodell, M., Houser, P. R., Jambor, U., Gottschalck, J., Mitchell, K., Meng, C. J., et al. (2004). The global land data assimilation system. *Bulletin America Meteorology Social*, *85*(3), 381–394. https://doi.org/10.1175/bams-85-3-381

Rogers, A., Medlyn, B. E., & Dukes, J. S. (2014). Improving representation of photosynthesis in Earth System Models. *New Phytologist*, *204*(1), 12–14. https://doi.org/10.1111/nph.12972

Saji, N. H., Goswami, B. N., Vinayachandran, P. N., & Yamagata, T. (1999). A dipole mode in the tropical Indian Ocean. *Nature*, *401*(6751), 360–363. https://doi.org/10.1038/43854

Saji, N. H., & Yamagata, T. (2003). Possible impacts of Indian Ocean Dipole mode events on global climate. *Climate Research*, *25*, 151–169. https://doi.org/10.3354/cr025151

Senf, C., Buras, A., Zang, C. S., Rammig, A., & Seidl, R. (2020). Excess forest mortality is consistently linked to drought across Europe. *Nature Communications*, *11*(1), 6200. https://doi.org/10.1038/s41467-020-19924-1

Sitch, S., Friedlingstein, P., Gruber, N., Jones, S. D., Murray-Tortarolo, G., Ahlstrom, A., et al. (2015). Recent trends and drivers of regional sources and sinks of carbon dioxide. *Biogeosciences*, *12*(3), 653–679. https://doi.org/10.5194/bg-12-653-2015

Stovall, A. E. L., Shugart, H., & Yang, X. (2019). Tree height explains mortality risk during an intense drought. *Nature Communications*, *10*(1), 4385. https://doi.org/10.1038/s41467-019-12380-6

Takahashi, T., Sutherland, S. C., Wanninkhof, R., Sweeney, C., Feely, R. A., Chipman, D. W., et al. (2009). Climatological mean and decadal change in surface ocean pCO2, and net sea–air $CO_2$ flux over the global oceans. *Deep Sea Research Part II: Topical Studies in Oceanography*, *56*(8–10), 554–577. https://doi.org/10.1016/j.dsr2.2008.12.009

Ummenhofer, C. C., England, M. H., McIntosh, P. C., Meyers, G. A., Pook, M. J., Risbey, J. S., et al. (2009). What causes southeast Australia's worst droughts? *Geophysical Research Letters*, *36*(4), L04706. https://doi.org/10.1029/2008gl036801

van der Velde, I. R., van der Werf, G. R., Houweling, S., Maasakkers, J. D., Borsdorff, T., Landgraf, J., et al. (2021). Vast $CO_2$ release from Australian fires in 2019–2020 constrained by satellite. *Nature*, *597*(7876), 366–369. https://doi.org/10.1038/s41586-021-03712-y

van der Werf, G. R., Randerson, J. T., Giglio, L., van Leeuwen, T. T., Chen, Y., Rogers, B. M., et al. (2017). Global fire emissions estimates during 1997–2016. *Earth System Science Data*, *9*(2), 697–720. https://doi.org/10.5194/essd-9-697-2017

Vuichard, N., Messina, P., Luyssaert, S., Guenet, B., Zaehle, S., Ghattas, J., et al. (2019). Accounting for carbon and nitrogen interactions in the global terrestrial ecosystem model ORCHIDEE (trunk version, rev 4999): Multi-scale evaluation of gross primary production. *Geoscientific Model Development*, *12*(11), 4751–4779. https://doi.org/10.5194/gmd-12-4751-2019

Wang, J., Liu, Z., Zeng, N., Jiang, F., Wang, H., & Ju, W. (2020). Spaceborne detection of $XCO_2$ enhancement induced by Australian mega-bushfires. *Environmental Research Letters*, *15*(12), 124069. https://doi.org/10.1088/1748-9326/abc846

Wang, J., Wang, M., Kim, J., Joiner, J., Zeng, N., Jiang, F., et al. (2021). Modulation of land photosynthesis by the Indian Ocean dipole: Satellite-based observations and CMIP6 future projections. *Earth's Future*, *9*(4), e2020EF001942. https://doi.org/10.1029/2020ef001942

Wang, J., Zeng, N., & Wang, M. (2016). Interannual variability of the atmospheric $CO_2$ growth rate: Roles of precipitation and temperature. *Biogeosciences*, *13*(8), 2339–2352. https://doi.org/10.5194/bg-13-2339-2016

Wang, J., Zeng, N., Wang, M., Jiang, F., Chen, J., Friedlingstein, P., et al. (2018). Contrasting interannual atmospheric $CO_2$ variabilities and their terrestrial mechanisms for two types of El Niños. *Atmospheric Chemistry and Physics*, *18*(14), 10333–10345. https://doi.org/10.5194/acp-18-10333-2018

Wang, J., Zeng, N., Wang, M., Jiang, F., Wang, H., & Jiang, Z. (2018). Contrasting terrestrial carbon cycle responses to the 1997/98 and 2015/16 extreme El Niño events. *Earth System Dynamics*, *9*(1), 1–14. https://doi.org/10.5194/esd-9-1-2018

Whitaker, J. S., & Hamill, T. M. (2002). Ensemble data assimilation without perturbed observations. *Monthly Weather Review*, *130*(7), 1913–1924. https://doi.org/10.1175/1520-0493(2002)130<1913:edawpo>2.0.co;2

Williams, C. A., & Hanan, N. P. (2011). ENSO and IOD teleconnections for African ecosystems: Evidence of destructive interference between climate oscillations. *Biogeosciences*, *8*(1), 27–40. https://doi.org/10.5194/bg-8-27-2011

Yuan, W., Liu, D., Dong, W., Liu, S., Zhou, G., Yu, G., et al. (2014). Multiyear precipitation reduction strongly decreases carbon uptake over northern China. *Journal of Geophysical Research: Biogeosciences*, *119*(5), 881–896. https://doi.org/10.1002/2014jg002608

Yue, X., & Unger, N. (2015). The Yale interactive terrestrial biosphere model version 1.0: Description, evaluation and implementation into NASA GISS ModelE2. *Geoscientific Model Development*, *8*(8), 2399–2417. https://doi.org/10.5194/gmd-8-2399-2015

Zaehle, S., & Friend, A. D. (2010). Carbon and nitrogen cycle dynamics in the O-CN land surface model: 1. Model description, site-scale evaluation, and sensitivity to parameter estimates. *Global Biogeochemical Cycles*, *24*, GB1006. https://doi.org/10.1029/2009gb003521

Zeng, N., Mariotti, A., & Wetzel, P. (2005). Terrestrial mechanisms of interannual $CO_2$ variability. *Global Biogeochemical Cycles*, *19*(1), GB1016. https://doi.org/10.1029/2004gb002273

Zeng, N., & Neelin, J. D. (1999). A land–atmosphere interaction theory for the tropical deforestation problem. *Journal of Climate*, *12*(3), 857–872. https://doi.org/10.1175/1520-0442(1999)012<0857:alaitf>2.0.co;2

Zscheischler, J., Michalak, A. M., Schwalm, C., Mahecha, M. D., Huntzinger, D. N., Reichstein, M., et al. (2014). Impact of large-scale climate extremes on biospheric carbon fluxes: An intercomparison based on MsTMIP data. *Global Biogeochemical Cycles*, *28*(6), 585–600. https://doi.org/10.1002/2014gb004826

## References From the Supporting Information

Crowell, S., Baker, D., Schuh, A., Basu, S., Jacobson, A. R., Chevallier, F., et al. (2019). The 2015–2016 carbon cycle as seen from OCO-2 and the global in situ network. *Atmospheric Chemistry and Physics*, *19*(15), 9797–9831. https://doi.org/10.5194/acp-19-9797-2019

OCO-2 Science Team, Gunson, M., & Eldering, A. (2020). *OCO-2 Level 2 bias-corrected $XCO_2$ and other select fields from the full-physics retrieval aggregated as daily files, Retrospective processing V10r*. Goddard Earth Sciences Data and Information Services Center (GES DISC). https://doi.org/10.5067/E4E140XDMPO2

Peiro, H., Crowell, S., Schuh, A., Baker, D. F., O'Dell, C., Jacobson, A. R., et al. (2022). Four years of global carbon cycle observed from the Orbiting Carbon Observatory 2 (OCO-2) version 9 and in situ data and comparison to OCO-2 version 7. *Atmospheric Chemistry and Physics*, *22*(2), 1097–1130. https://doi.org/10.5194/acp-22-1097-2022